# Modeling Inertial Deposition of Aerosol Particles in Geometrically Complicated Flow Systems Using Finite Element Methods

Patrick Grahn[1] and Joel Kuula[2,3]

[1]Department of Physics, University of Helsinki, Helsinki, 00560, Finland
5   [2]Department of Chemistry, University of Helsinki, Helsinki, 00560, Finland
[3]Atmospheric Composition Research, Finnish Meteorological Institute, Helsinki, 00560, Finland

*Correspondence to*: Patrick Grahn (patrick.jh.grahn@helsinki.fi)

**Abstract.** This work presents a modeling approach for calculating the trajectories of aerosol particles in geometrically
10   complicated flow systems. The finite-element based modeling is first validated by comparing the calculated inertial deposition
with literature values for two cases of laminar flow: a 90-degree bend and an abrupt contraction of a pipe. The approach is
then applied on a multi-part aerosol instrument used for Cantilever-Enhanced-Photo-Acoustic-Spectroscope (CEPAS)
measurements. The particle transmission of the CEPAS is experimentally measured and compared to the modeling results. It
is demonstrated that the model provides valuable insight on the inertial deposition losses by pinpointing their physical locations
15   within the measurement instrument.

## 1 Introduction

The deposition of aerosol particles, which refers to a phenomenon where particles are driven and permanently adhered to
nearby walls or surfaces, has been studied theoretically and experimentally for decades (Belyaev & Levin, 1974; Friedlander
& Johnstone, 1957; Tian & Ahmadi, 2007). This is due to its importance in many different applications; for example, in
20   atmospheric sciences the characterization of sampling losses of measurement instruments is a prerequisite to representative
quantification of particle concentrations in ambient air (Hangal & Willeke, 1990; Kumar et al., 2008; Okazaki et al., 1987).
With respect to human health, particle deposition in the human respiratory system is an important field of study as exposure
to particles is highly correlated with morbidity and premature deaths, and not all the mechanisms behind these are fully
understood (Abbafati et al., 2020; Chen & Hoek, 2020; Lelieveld et al., 2020). To add, the COVID-19 pandemic further
25   underlined the need to understand particle deposition in human airways in terms of both the pathogen deposition as well as the
dosimetry of inhaled drugs (Chaurasiya & Zhao, 2021; Drossinos & Stilianakis, 2020; Zuo et al., 2020). Particle deposition is
important also in many different industrial applications ranging from gas filtration to material separation processes, for
example (e.g. Liu et al., 2022; Yu et al., 2023).

30    Particle deposition can be driven by a variety of different forces including inertial, diffusion, and electrostatic forces (Kulkarni et al., 2011). In general, larger particles are predominantly affected by inertial forces whereas smaller particles are subjected to diffusion and electrostatic forces. Estimation of sampling losses can be done using a theoretical or experimental approach. Theoretical approach includes first-order kinetics based on fitted experimental loss coefficients (Hapidin et al., 2019) and use of Computational Fluid Dynamics (CFD) modeling in combination with particle tracking (Granek et al., 2003). Experimental

35    characterization can be done by comparing the measured concentration of particles flowing through the system to that of the concentrations when bypassing the system (e.g. Reineking & Porstendörfer, 1986). Another way to quantify deposition losses is to use a fluorescence trace dye on particles and first visually inspect and then measure the concentration of dye found on washed system parts. This way the location as well as the number of deposited particles can be estimated (e.g. Ren et al., 2022).

40

This work showcases a finite-element based method to calculate inertial deposition losses of particles in sampling lines using three different case examples. The cases include two relatively simple configurations of a bent section and an abrupt contraction of a pipe. The third case includes a multi-part aerosol instrument used for photoacoustic measurements. The photoacoustic technique has been shown to be well-suited for atmospheric measurements of particulate matter (Linke et al., 2016; Karhu et

45    al., 2021). The instrument measures optically the particle concentration in the center of the flow system and, therefore, it is important to know the inertial deposition losses and where they occur. For case examples one and two, the modeled sampling losses are compared to those of literature values. For the third case, the modeling results are compared to those obtained experimentally.

## 2 Numerical modeling of inertial deposition loss

50    For simple geometries, sampling losses can be predicted using known formulas that have been previously published. Many such formulas are available in the "AeroCalc" Excel spreadsheet based on Baron & Willeke (2001) and included in the software tool "Particle Loss Calculator" (Von Der Weiden et al., 2009). However, for arbitrary complicated multi-part systems, no known formulas exist and one needs to resort to 3D numerical modeling. In order for a numerical method to be considered reliable, it needs to be able to produce results for simple systems that are in agreement with the known analytical formulas.

55    ### 2.1 Case examples

In this work, we present a method to calculate inertial deposition using three different examples. The first two examples are simple geometries which are based on setups reported in earlier literature (Pui et al., 1987; Ye & Pui, 1990). The third example considers a multi-part aerosol instrument used for Cantilever-Enhanced-Photo-Acoustic-Spectroscope (CEPAS) measurements. In all cases, our method calculates the trajectories of particles in a flow system, from which one can evaluate

the transmission, which is equal to the fraction of particles that reached the system outlet. Particles are assumed spherical, and their diameter is varied through a range of values. The background fluid is air at standard temperature and pressure.

The transmission is often reported as a function of the Stokes number. Different definitions of the Stokes number can be found in the literature. For example, it can be defined with respect to either a pipe radius or diameter. In this work, our flow channels have circular cross-sections at the inlet and outlet. We choose to define the Stokes number with respect to the inside diameter of the outlet $D$ by

$$\text{Stk} = C \frac{\rho_p d_p^2}{18\mu} \frac{U_{\text{ave}}}{D},$$ (1)

where $\rho_p$ and $d_p$ are the density and diameter of the particles, respectively. The fluid has a dynamic viscosity $\mu$. The average flow velocity $U_{\text{ave}}$ is evaluated at the inlet. Equation (1) also contains the slip correction factor $C$ that is given by the Cunningham-Millikan-Davies model

$$C = 1 + \text{Kn} \cdot \left( C_1 + C_2 e^{-C_3/\text{Kn}} \right),$$ (2)

where Kn is the Knudsen number and the coefficients have values $C_1 = 1.142$, $C_2 = 0.558$ and $C_3 = 0.999$ (Allen & Raabe, 1985). The particle Knudsen number can be calculated by

$$\text{Kn} = 2 \frac{\mu}{d_p} \sqrt{\frac{\pi}{2\rho_0 p_0}},$$ (3)

which is evaluated for air at atmospheric pressure $p_0 = 101.3 \text{ kPa}$, having a dynamic viscosity $\mu = 1.814 \cdot 10^{-5}$ Pa·s and density $\rho_0 = 1.2 \text{ kg/m}^3$.

### 2.1.1 Loss in a bent section of a pipe

The first example considers particles flowing through a bent pipe. The pipe has a circular cross-section and has a 90-degree bend. Pui et al. (1987) defines several experimental test cases of inertial deposition in such a bent pipe. We consider the case with a pipe inside diameter of 5 mm, curvature ratio of 5.7 and flow Reynolds number of 1000. The curvature ratio is defined as the bend's radius of curvature divided by the inside radius of the pipe cross-section. The particles have a density of $\rho_p = 1 \text{ g/cm}^3$.

Inertial deposition in a bent pipe for laminar flow conditions were measured by Pui et al. (1987). An empirical fit to this data was presented in Kulkarni (2011) through the equation

$$\eta = \left( 1 + \left( \frac{\text{Stk}}{0.171} \right)^{\frac{0.452 \cdot \text{Stk}}{0.171} + 2.242} \right)^{-2\theta/\pi},$$ (4)

where the transmission $\eta$ is expressed through the Stokes number Stk and angle of the bend $\theta$. This case example was recently investigated by Feng (2023) who reported a very good agreement with the data of Pui et al. (1987).

The "AeroCalc" Excel spreadsheet (Willeke & Baron, 2001) uses an older equation by Crane & Evans (1977), which is:

90 $$\eta = 1 - \text{Stk} \cdot \theta \,. \tag{5}$$

For the bent pipe, we compare the results of our numerical method to the predictions provided by both Eqs. (4) and (5).

### 2.1.2 Loss at an abrupt contraction

The second example considers a pipe that is connected to a narrower pipe by an abrupt contraction. Both pipes have a circular cross-section and a contraction ratio equal to 2 is considered. The contraction ratio is the inside diameter of the inlet pipe

95 divided by the inside diameter of the outlet pipe. The problem setup is described in Ye et al. (1990). We consider the inlet pipe to have an inside diameter of 5 mm and a flow Reynolds number of 1000. The particles have a density of $\rho_\text{p} = 1 \text{ g/cm}^3$.

If the particle distribution at the inlet follows the fully-developed laminar flow profile, then we can use the following equation for transmission that is presented in Ye & Pui (1990):

100 $$\eta = 1 - \left\{ \left[ 1 - \left( \frac{D_\text{o}}{D_\text{i}} \right)^2 \right] [1 - \exp(1.721 - 8.557x + 2.227x^2)] \right\}^2, \tag{6}$$

where $D_\text{o}$ and $D_\text{i}$ are the inside diameters of the outlet and inlet pipes, respectively. The intermediate parameter $x$ depends on the Stokes number by the equation

$$x = \left( \frac{D_\text{o}}{D_\text{i}} \right)^{0.31} \sqrt{\text{Stk}}. \tag{7}$$

The Stokes number used in Eq. (7) is defined using $D_\text{o}$ in place of $D$ in Eq. (1). The fit provided by Eq. (6) is only valid when

105 $x < 1.95$. For larger values of $x$, the transmission is set to the constant value

$$\eta = 1 - \left[ 1 - \left( \frac{D_\text{o}}{D_\text{i}} \right)^2 \right]^2 . \tag{8}$$

For values of $x < 0.213$, the transmission is set to 100 %. For the abrupt contraction, we compare the results of our numerical method to the prediction provided by Eq. (6).

### 2.1.3 Loss in a multi-part aerosol instrument

110 The final example considers particles flowing through a geometrically complicated multi-part aerosol instrument. The geometry describes the flow channels of a CEPAS, which is a light absorption measurement instrument capable of measuring both gas- and particle-phased compounds (Karhu et al., 2021). The instrument was originally designed for gas-phased measurements, and its particle-phased losses are characterized here. The sampling system, including inlet and outlet pipes is shown in Fig. 1(a). In the system, the flow first encounters a 90-degree tube fitting used to fix the tubing to the sample cell

115  body. From there, the flow enters into a valve housing part and makes two consecutive 90-degree turns before reaching the acoustic sample chamber. The acoustic sample chamber is the long cylindrical pipe shown in the central-upper part of Fig. 1(a). At the end of the sample chamber, the flow encounters the same parts in reverse order, from which it flows to the outlet pipe. The inlet and outlet pipes have an inside diameter of 2.2 mm. A more detailed view of the tube fitting and valve housing part is shown in Fig. 1(b).

120

The experimental particle deposition measurements of the CEPAS sampling system were done by using an atomizer (model ATM 226, Topas GmbH, Germany) to generate NH4NO3 sample particles (density of 1720 kg/m$^3$) and then feeding them either through the CEPAS or through a bypass line to a particle number concentration counter (Condensation Particle Counter model 3776, TSI Inc., USA). The ratio between the measured particle concentrations fed through the CEPAS and through the

125  bypass line was calculated to be the transmission efficiency of particles. Measurements were carried out for six different particle sizes (50, 100, 200, 300, 400 and 500 nm) by using a particle size classifier (Differential Mobility Analyzer 3080, TSI Inc., USA) in line after the atomizer. Sample flow through the system was 1.5 l/min. An individual measurement point was obtained by feeding particles through the system and manually operating a three-way valve between the CEPAS and bypass lines; once the measured particle concentration stabilized at a given measurement point, the three-way valve was switched,

130  and the measurement was then repeated again. Measuring concentrations both through the CEPAS and bypass lines constituted as a single measurement point. Measurements were repeated five times for all particle sizes altogether. TSI's AIM software (version 10) was used to record the particle number concentration readings.

In the modeling, we adopt the parameters for the flow and particles used in the measurements. This is done to be able to

135  compare model and experimental results. The modeled air flow has a constant-valued volumetric flow rate of 1.5 l/min, which corresponds to a flow Reynolds number that is smaller than 1000. The flow carries NH4NO3 particles of varying size. We assume the density of NH4NO3 particles to be $\rho_\mathrm{p} = 1720$ kg/m$^3$ and the shape of the particles to be spherical. The particle diameter is varied between 50 nm and 500 nm.

(a)

(b)

140
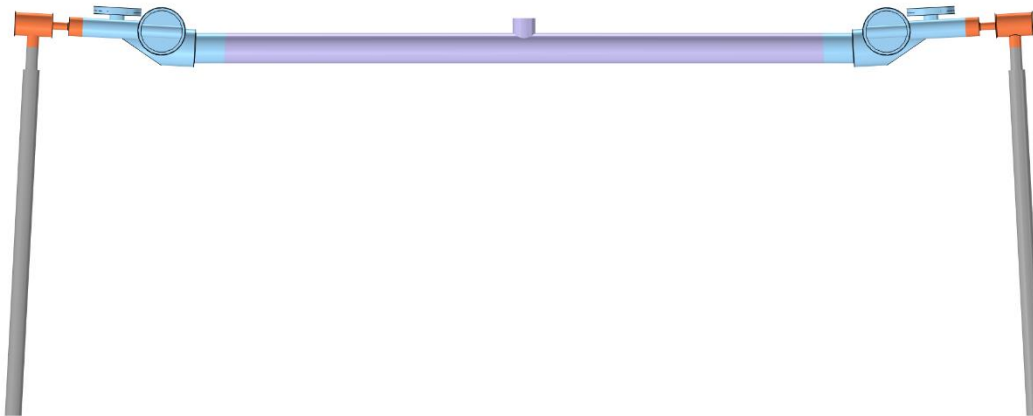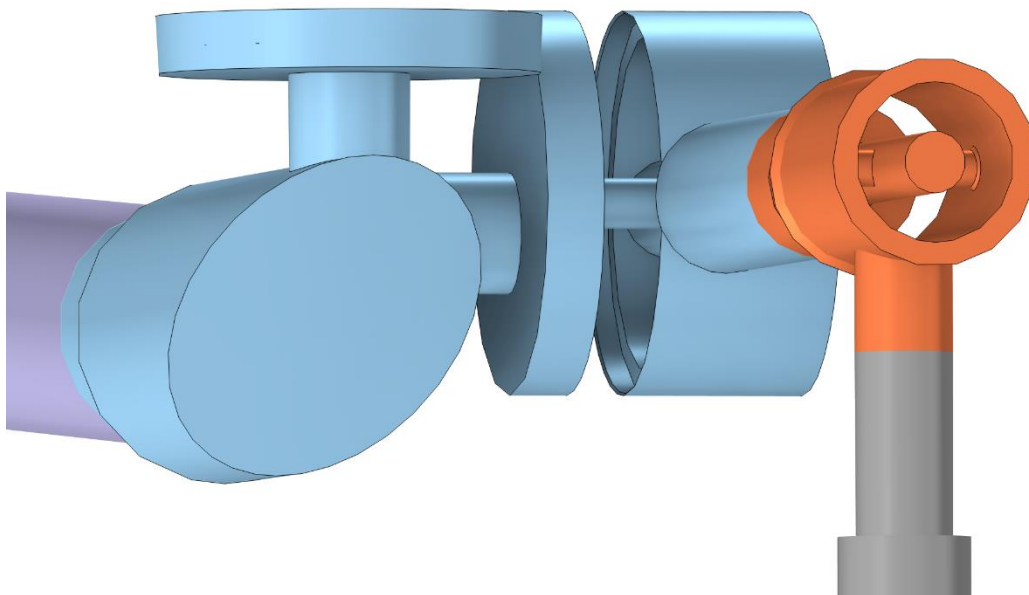
**Figure 1: Flow channels of a multi-part aerosol instrument. (a) The entire system is shown, where flow enters from the grey inlet pipe in the lower-left corner and exits at the grey outlet pipe in the lower-right corner. The 90-degree tube fittings are marked by orange color. The valve housing part including two 90-degree turns are marked by light blue color. The acoustic sample chamber is**
145 **marked by violet color. (b) A magnified image shows the tube fitting and valve housing part. All shown parts are fluid domains.**

## 2.2 Computing the flow field

The flow field is calculated by solving the incompressible Navier-Stokes equations

$$\rho_0 \frac{\partial \mathbf{u}}{\partial t} + \rho_0 (\mathbf{u} \cdot \nabla)\mathbf{u} = -\nabla p + \mu \nabla^2 \mathbf{u}, \tag{9}$$

150

$$\rho_0 \nabla \cdot \mathbf{u} = 0, \tag{10}$$

for the flow velocity $\mathbf{u}$ and relative pressure $p$. We consider the fluid density $\rho_0$ and dynamic viscosity $\mu$ to be constant-valued material parameters. The equations are solved using the Finite Element Method (FEM) in COMSOL Multiphysics® version 6.2. The software has built-in numerical stabilization (streamline and crosswind diffusion) that is needed to solve the equations. A fully developed flow corresponding to a known volumetric flow rate is prescribed at the inlet and the condition $p = 0$ is

155 prescribed at the outlet. A no-slip wall condition, $\mathbf{u} = 0$, is prescribed on all solid boundaries. We evaluated the flow Reynolds numbers to be close to 1000 in all case examples. This means that the flow regime is either laminar or transitional. No turbulence model has to be used. In the transitional regime, the flow can be calculated by the transient laminar Eqs. (9) and (10), but it may not have a steady-state solution. This transient laminar flow regime was previously observed in Novosselov et al. (2014), where they simulated inertial deposition in curved flow channels. They reported that comparison between

160 transient laminar and detached eddy simulations showed less than a 5 % difference in particle deposition for flow Reynolds numbers less than 2300. We use a time-dependent solver employing a scheme of Backward Differentiation Formula (BDF). This is the default solver in the software. In order to improve convergence of the time-dependent solver, the volumetric flow rate is prescribed as a smoothed step-function that grows from zero to the desired value over a finite time. Only the flow field at the final time is used for the subsequent particle trajectories calculation.

165

FEM is based on dividing the geometrical domains into mesh elements. Within each element, the dependent variables $\mathbf{u}$ and $p$ are expressed by polynomials. We use the so-called P1+P1 formulation, which indicates that both $\mathbf{u}$ and $p$ are linear polynomials. The numerical stabilization algorithm adds diffusion locally to each mesh element. The smaller the mesh element, the less diffusion is added. We observed that when reducing the mesh element size, it becomes increasingly difficult for the

170 solution to converge. This can be understood as a consequence of the reduction in local numerical diffusion, which causes the flow solution to lose stability. This is problematic, since we observed that a very small mesh element size is required for the subsequent particle trajectories calculation to be accurate. For the geometrically complicated multi-part aerosol instrument, the fluid flow computation failed to converge with a fine mesh. We were able to overcome this failure by initially solving the fluid flow model with a coarser mesh (2.2 million volumetric elements) and then use the obtained solution as initial values for

175 a second computation with a fine mesh (18.8 million volumetric elements). In the second computation, the time-dependent solver calculated a time interval of 0.1 milliseconds by taking 32 time steps. For the bent-tube and abrupt-contraction models, convergence was achieved directly using the desired fine mesh.

### 2.3 Computing particle trajectories

The trajectories of particles are computed using Newtonian particle tracing within the same model that computed the flow

180 field. We release 1000 particles at the flow inlet and compute their trajectories using a time-dependent solver employing the

generalized-alpha scheme (this is the default solver in the software). The particles are given an initial velocity equal to the

local fluid flow velocity and their spatial distribution at the inlet is proportional to the magnitude of the local fluid flow velocity.

The particles are subject to a drag force by the fluid. The drag force used in the model is

$$\mathbf{F} = \frac{1}{\tau C} m_{\mathrm{p}} (\mathbf{u} - \mathbf{v}) \,, \tag{11}$$

185 where $\mathbf{v}$ is the particle velocity, $m_{\mathrm{p}}$ is the particle mass and the slip correction factor $C$ is defined in Eq. (2). The particle

velocity response time $\tau$ is defined as

$$\tau = 4\rho_{\mathrm{p}} d_{\mathrm{p}}^2 / (3\mu C_{\mathrm{D}} \mathrm{Re}_{\mathrm{r}}) \,, \tag{12}$$

where the relative Reynolds number is

$$\mathrm{Re}_{\mathrm{r}} = \rho_0 |\mathbf{u} - \mathbf{v}| d_{\mathrm{p}} / \mu \,. \tag{13}$$

190 The drag coefficient $C_{\mathrm{D}}$ is set to be a piecewise function of the relative Reynolds number using the option Standard Drag

Correlations in the particle tracing module of COMSOL Multiphysics version 6.2.

Particles are set to stop upon collision with a wall. Only particles that have passed from flow inlet to outlet without any wall

collisions are considered as transmitted. The system transmission is defined as the ratio of particles reaching the outlet relative

195 to the total amount of particles released at the inlet. The particles that stopped at a wall can be visualized by the software to

observe where the losses occur. The software also has a summation operator that allows evaluating the number of particles

residing within each geometrical domain at any given instance of time.

### 3 Results and discussion

The calculations were performed using a desktop computer with AMD Ryzen 9 7900X 12-Core Processor (base speed 4.7

200 GHz) and 128 GB of DDR5 RAM. The number of mesh elements that could be used in the fluid flow calculation was limited

by the available RAM. In the particle trajectories calculation, the total number of particles and the solver's time-step size were

chosen such that the calculation time with the employed processor would be convenient. For the model of the multi-part aerosol

instrument, a convenient calculation time was decided to be about one day.

## 3.1 Results for loss in a bent section of a pipe

A mesh consisting of 237 783 volumetric elements was used, resulting in a calculation time of 13 minutes for the flow field and 7 minutes for the particle trajectories. The particle trajectories were computed sequentially for particles of 24 different diameters. The calculated velocity magnitude distribution is shown in Fig. 2. We observe that the flow profile is laminar in the straight portions. The effect of inertia makes the flow curve towards the outer surface at the location of the bend. A cross-sectional cut of the mesh is also shown in Fig. 2. The tetrahedrons are larger in the central portion of the pipe. The thicker lines seen at the boundaries contain a boundary layer mesh consisting of ten layers of prism elements.
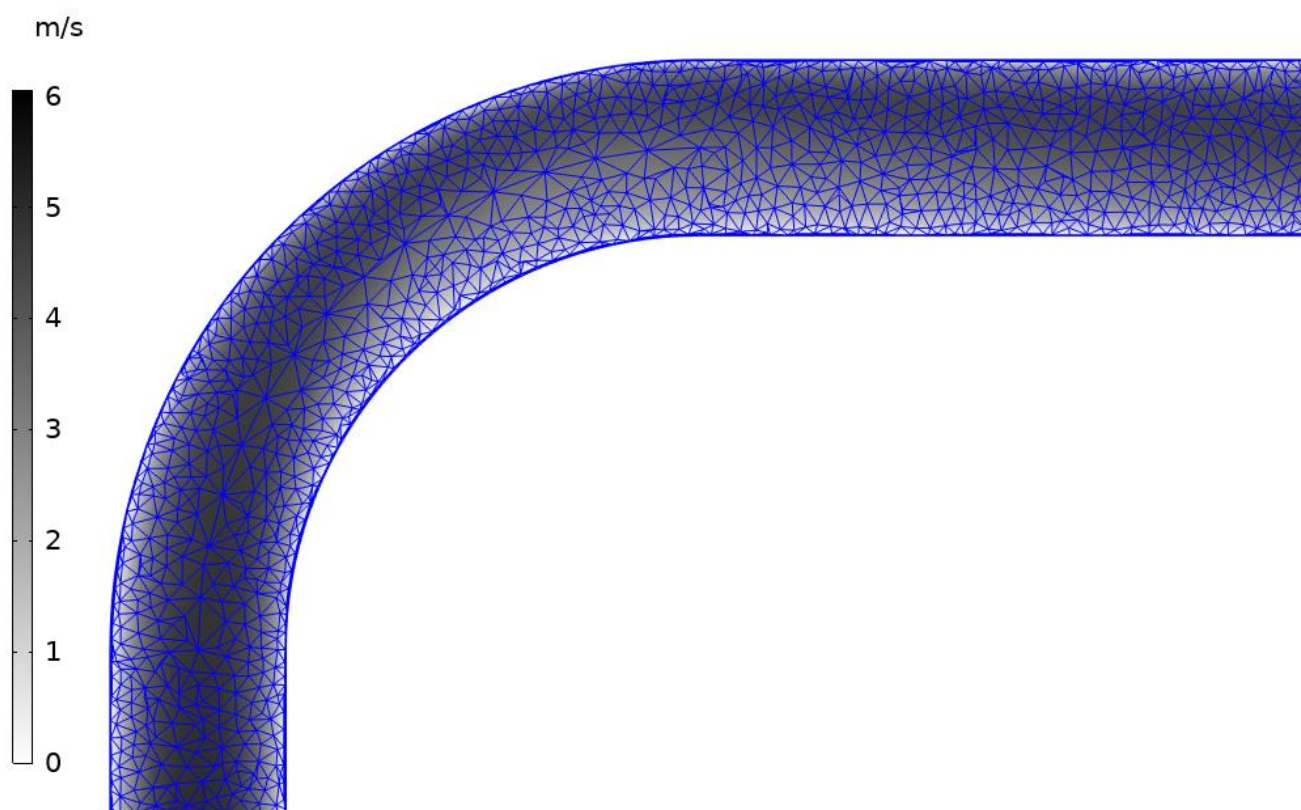
**Figure 2: Computed velocity magnitude distribution within the plane of symmetry of the bent section of a pipe described in section 2.1.1. The flow enters from the lower-left part and exits at the upper-right part of the figure. The edges of the mesh elements within this plane of symmetry are shown by blue lines.**

The calculated transmission as a function of particle diameter is shown in Fig. 3 by the blue curve. We observe that the results follow closely to Eq. (4) that is a fit to the experiments performed by Pui et al. (1987). Equation (5) by Crane & Evans (1977) produces results that deviate significantly from our method.
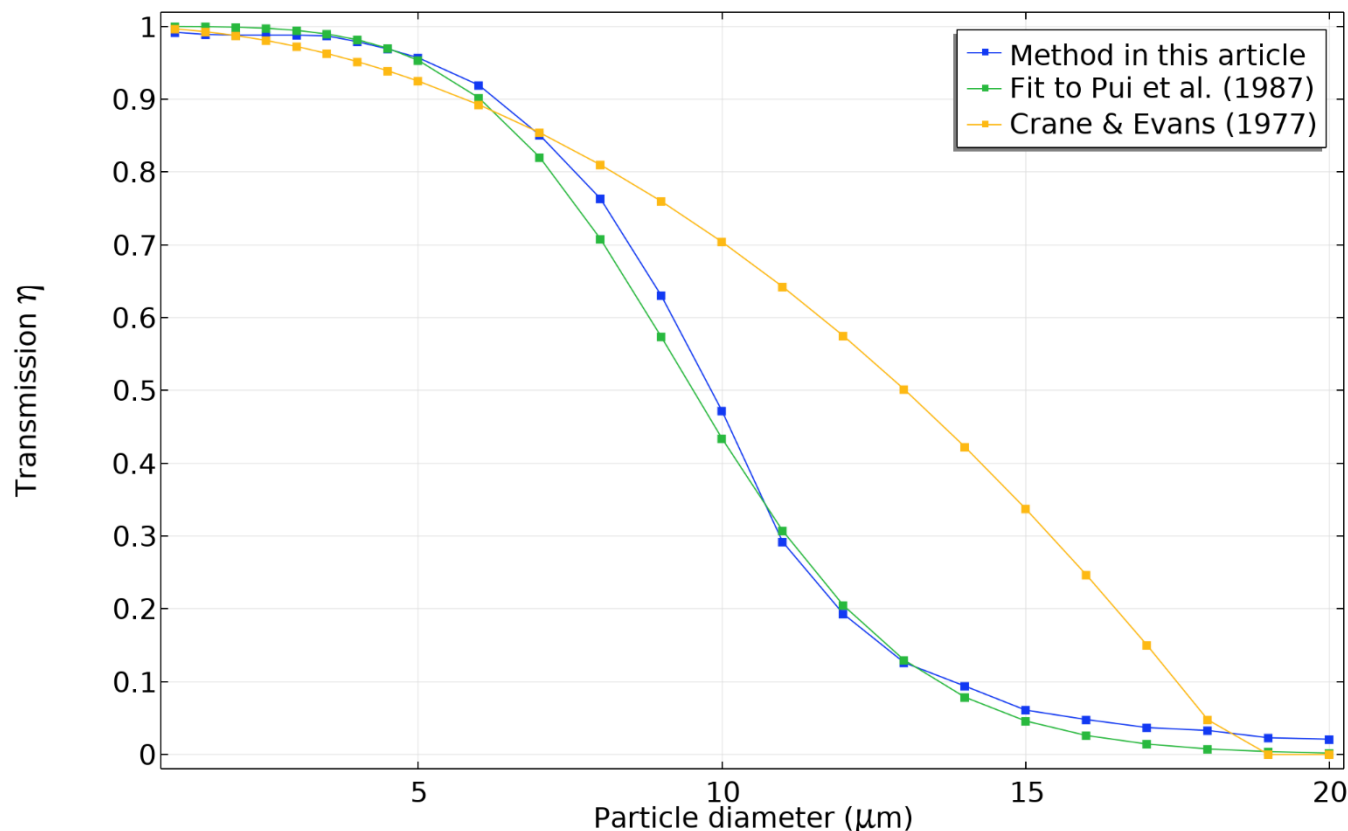
**Figure 3: Transmission of particles through the bent section of a pipe described in section 2.1.1. as a function of particle diameter. The data obtained using the method presented in this article is shown by the blue curve. The green curve shows data obtained by Eq. (4). The yellow curve shows data obtained by the Eq. (5).**

225

## 3.2 Results for loss at an abrupt contraction

A mesh consisting of 475 666 volumetric elements was used, resulting in a calculation time of 16 minutes for the flow field and 3 minutes for the particle trajectories. The particle trajectories were computed sequentially for particles of 9 different diameters. The calculated velocity magnitude distribution is shown in Fig. 4. We observe that the flow profile is laminar in the straight portions. However, at the location of the contraction, the velocity magnitude is increased near the contraction corner. In order for the subsequent particle tracing to be accurate, it is important that the mesh accurately resolves the flow distribution near the corner. A cross-sectional cut of the mesh is also shown in Fig. 4. The thicker lines seen at the boundaries contain a boundary layer mesh consisting of ten layers of prism elements.
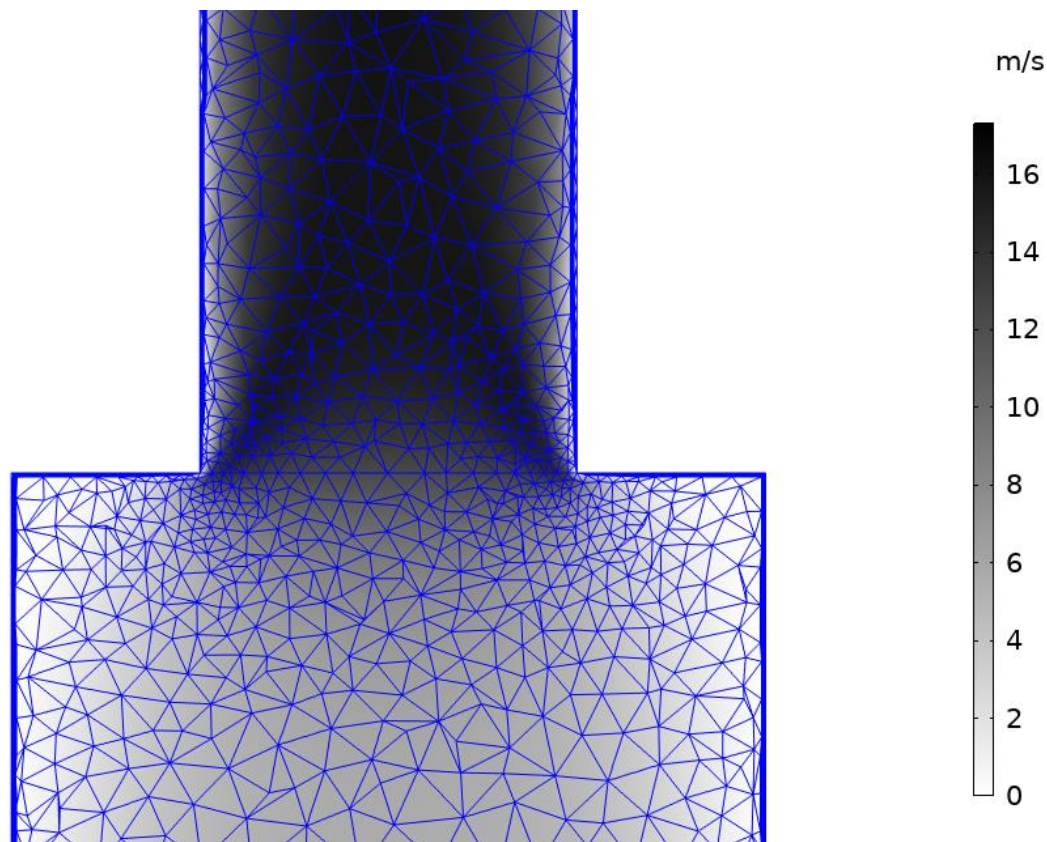
235 **Figure 4: Computed velocity magnitude distribution within the plane of symmetry of the abrupt contraction described in section 2.1.2. The flow enters from the lower part and exits at the upper part of the figure. The edges of the mesh elements within this plane of symmetry are shown by blue lines.**

The calculated transmission as a function of particle diameter is shown in Fig. 5 by the blue curve. We observe that the results

240    follow closely to Eq. (6) derived in Ye & Pui (1990). Their model also considered inertial interception, which is not included

in our method. However, they found that interception only had a minor effect.
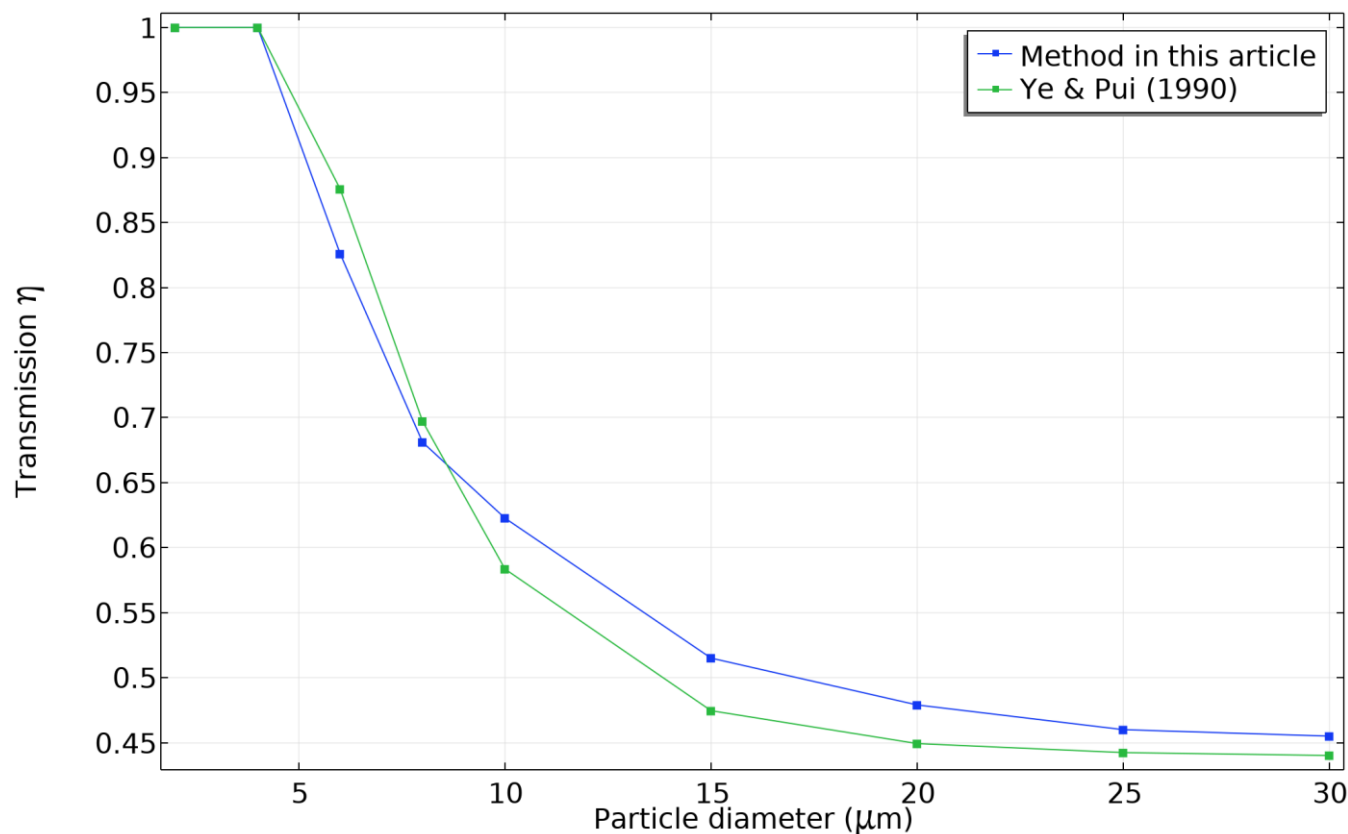
**Figure 5: Transmission of particles through the abrupt contraction described in section 2.1.2. as a function of particle diameter. The data obtained using the method presented in this article is shown by the blue curve. The green curve shows data obtained by Eq. (6).**

245

### 3.3 Results for loss in a multi-part aerosol instrument

The initial flow field with a coarser mesh of 2.2 million volumetric elements had a calculation time of 14 minutes. The subsequent flow field calculation with a finer mesh of 18.8 million volumetric elements was run for 12 hours and 44 minutes, corresponding to 32 timesteps taken by the solver. During the computation, 108 GB of RAM was used during the most

250 memory-intensive part. The flow resolved by the finer mesh was observed to be in the transitional regime. The flow field at the final time step was considered representative of the flow and used for particle trajectories calculation. The particle trajectories were computed sequentially for particles of 10 different diameters. The total calculation time for the trajectories was 20 hours and 46 minutes.

255 The calculated transmission as a function of particle diameter is shown in Fig. 6 by the blue curve. We can see that the transmission decreases monotonically with increasing particle size. The experimentally measured transmission is shown by

the green curve in Fig. 6. Both the calculated and measured curves reduce monotonically at similar rates within the considered range of particle diameters. This similarity confirms that the experimentally observed particle size dependence is dominated by inertial deposition. However, the measured loss curve begins at a lower level than the calculated one. For the smallest

260     particle diameter of 50 nm, the measured loss is already 18 %.
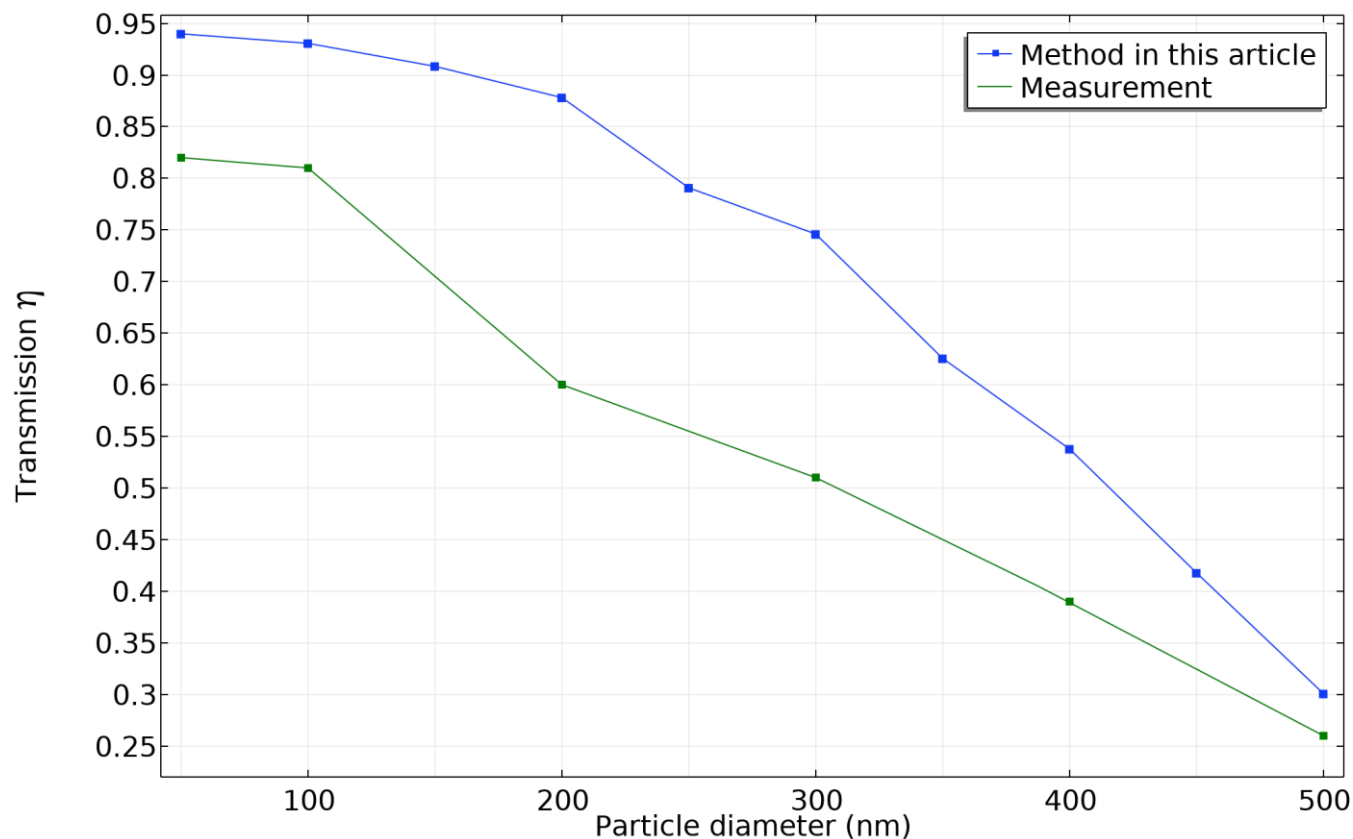
**Figure 6: Transmission of particles through the multi-part aerosol instrument as a function of particle diameter. The data obtained using the method presented in this article is shown by the blue curve. The green curve shows results from the measurements described in section 2.1.3.**

265     Common loss mechanisms not included in the calculations are diffusion and electrostatic forces. The sampling lines were made out of anti-static material to minimize influence of electrostatic forces. In order to estimate the contribution of diffusion, we used the analytical equation for a long tube in Gormley & Kennedy (1948) with a tube length set to be equivalent to our system. For the smallest particle diameter of 50 nm, the analytical equation predicts a loss of approximately 1 % only. For larger particles, the diffusion loss would be even less. Additionally, we carried out a second set of measurements without tube fittings

270     and with a reduced flow rate of 0.3 l/min. In these measurements, a constant loss of approximately 20 % was observed for all particle diameters up to 400 nm. Thus, it appears that measurements show a constant loss offset that is not caused by inertial deposition, electrostatic forces or diffusion. Upon closer inspection, we found out that the particle counter pump produced an under-pressure due to the large pressure drop of the flow through the CEPAS instrument. We believe this under-pressure

causes the counter to underestimate the particle concentrations, which results in the observed constant offset of the transmission
275    curve.

The numerical model also provides insight on the physical location where particles are lost to inertial deposition. In Fig. 7, the
loss is separated with respect to the geometrical part where it occurs. The localized inertial loss is here defined as the number
of particles deposited within the geometrical part divided by the number of particles released at the inlet pipe. Thus, the total
280    loss is the arithmetic sum of the localized losses. Figure 7 reveals that the main source of loss is the second 90-degree tube
fitting. As the particle diameter is increased beyond 200 nm, also the first tube fitting starts to collect particles on its walls.
Larger particles are also to a lesser extent deposited at the second valve housing. It can be observed that the loss is significantly
larger in the components occurring after the sample tube, even though the system geometry has mirror symmetry (see Fig. 1).
This is because inertial deposition is not symmetric with respect to reversal of flow direction.
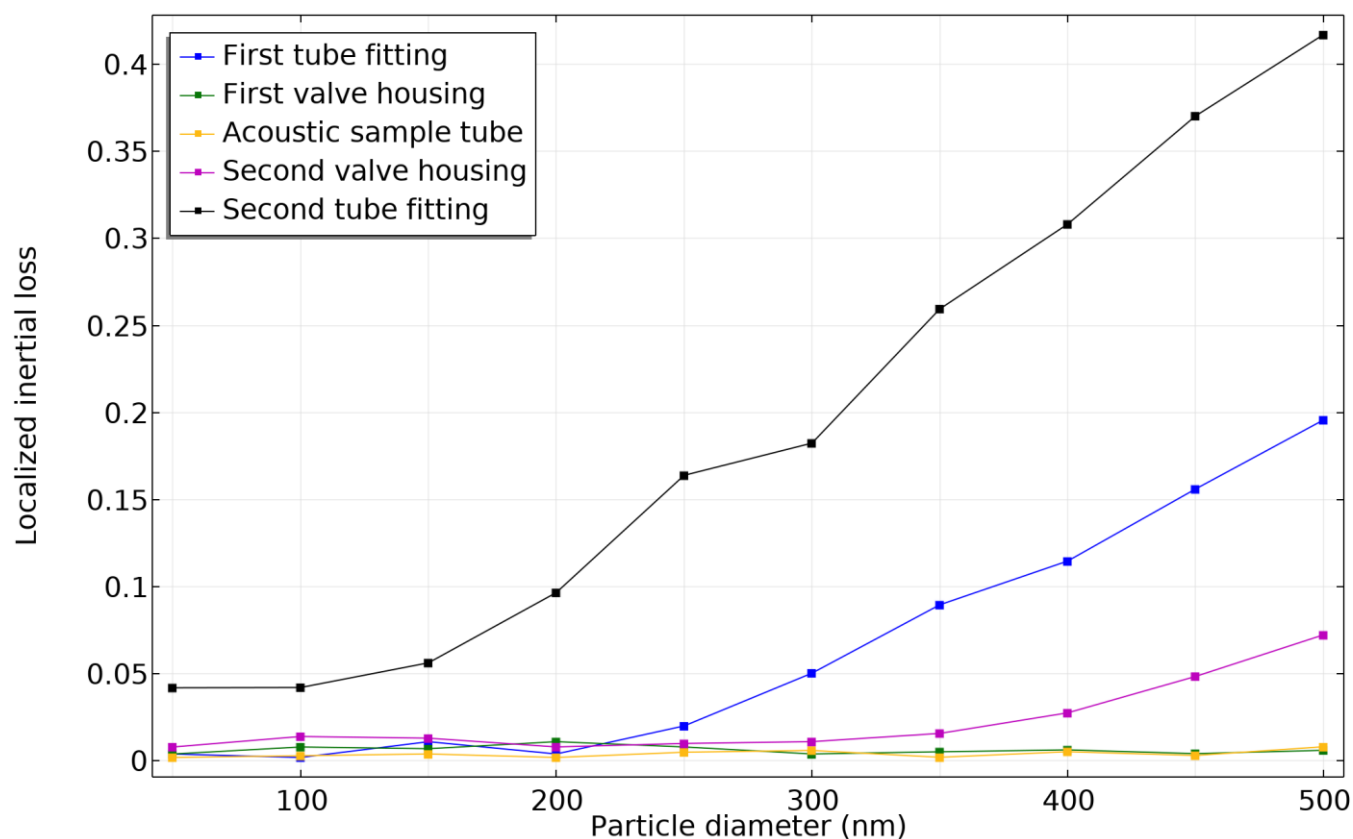
285

**Figure 7: Calculated particle inertial loss in the multi-part aerosol instrument as a function of particle diameter. The loss is divided with respect to the geometrical parts where they occur and shown with curves of different color. The geometrical location of each named part can be seen in Fig. 1.**

## 4 Conclusions

290 We have presented a finite-element based approach for calculating the transmission of aerosol particles through flow systems. The approach is able to model the inertial deposition in 3D systems of arbitrary geometrical shape. All case examples were in the laminar flow regime, but the models can be further developed to include turbulence models. The results shown in Sec. 3.1 and 3.2 were found to be in an agreement with previously published analytical formulas. This validates the approach. In Sec. 3.3., we applied the approach successfully for calculating the particle transmission in a geometrically complicated

295 photoacoustic measurement instrument. The used flow rate represents a high flow case. In practical use of the instrument, the flow may be lower, which would set the operation even deeper into the laminar regime. Experimental measurements demonstrated a similar dependence of the transmission on the particle size, but an offset was observed between the calculated and measured curves. The offset was suspected to be caused by the measurement setup.

300 The modeling of the photoacoustic measurement instrument allowed us to pinpoint the physical locations where the losses occur. This would have been difficult to perform experimentally, without having to disassemble the instrument. We found that more loss occurred at the outlet side, after the sample chamber, compared to the inlet side. This knowledge is useful, since losses occurring at the output side do not affect the photoacoustic excitation in the sample cell. However, the loss occurring in the tube fitting at the inlet side was found to be significant. We also performed measurements (not presented here) without

305 tube fittings and noticed significantly improved particle transmission.

Since the model is based on Newtonian particle tracing, the trajectories of individual particles can be observed. Therefore, we are able to study the distribution of particle concentration within the flow system. This is particularly helpful for photoacoustic instruments, where the optical absorption by the particles generates the photoacoustic signal. If particles have an

310 inhomogeneous distribution along the optical path, the photoacoustic signal may not accurately represent the average concentration of particles in the system. Further research should be carried out to investigate this effect.

## Code and data availability

Models including figure data are publicly available for the first and second case examples at the Zenodo online repository (https://doi.org/10.5281/zenodo.11003261, Grahn, 2024).

315 **Author contribution**

P.G.: Conceptualization; Methodology – Modeling; Software; Investigation and formal analysis; Writing – Original draft; Visualization

J.K.: Conceptualization; Methodology – Experimental; Investigation and formal analysis; Writing – Review & editing; Funding acquisition

320 **Competing interests**

The authors declare that they have no conflict of interest.

**Acknowledgements**

This work was supported by the Academy of Finland under grant 349544 and by the proof-of-concept funding from Jane and Aatos Erkko Foundation.

325 **References**

Abbafati, C., Abbas, K. M., Abbasi-Kangevari, M., Abd-Allah, F., Abdelalim, A., Abdollahi, M., Abdollahpour, I., Abegaz, K. H., Abolhassani, H., Aboyans, V., Abreu, L. G., Abrigo, M. R. M., Abualhasan, A., Abu-Raddad, L. J., Abushouk, A. I., Adabi, M., Adekanmbi, V., Adeoye, A. M., Adetokunboh, O. O., … Murray, C. J. L. (2020). Global burden of 87 risk factors in 204 countries and territories, 1990–2019: a systematic analysis for the Global Burden of Disease Study 330 2019. *The Lancet*, *396*(10258), 1223–1249. https://doi.org/10.1016/S0140-6736(20)30752-2

Allen, M. D., & Raabe, O. G. (1985). Slip correction measurements of spherical solid aerosol particles in an improved millikan apparatus. *Aerosol Science and Technology*, *4*(3), 269–286. https://doi.org/10.1080/02786828508959055

Baron, P. A., & Willeke, K. (2001). *Aerosol Measurement: Principles, Techniques, and Applications* (P. A. Baron & K. Willeke (eds.); Second Edi). John Wiley & Sons, Inc.

335 Belyaev, S. P., & Levin, L. M. (1974). Techniques for collection of representative aerosol samples. *Journal of Aerosol Science*, *5*(4), 325–338. https://doi.org/10.1016/0021-8502(74)90130-X

Chaurasiya, B., & Zhao, Y. Y. (2021). Dry powder for pulmonary delivery: A comprehensive review. *Pharmaceutics*, *13*(1), 1–28. https://doi.org/10.3390/pharmaceutics13010031

Chen, J., & Hoek, G. (2020). Long-term exposure to PM and all-cause and cause-specific mortality: A systematic review and 340 meta-analysis. *Environment International*, *143*(July), 105974. https://doi.org/10.1016/j.envint.2020.105974

Crane, R. I., & Evans, R. L. (1977). Inertial deposition of particles in a bent pipe. *Journal of Aerosol Science*, *8*(3), 161–170. https://doi.org/10.1016/0021-8502(77)90003-9

Drossinos, Y., & Stilianakis, N. I. (2020). What aerosol physics tells us about airborne pathogen transmission. *Aerosol Science and Technology*, *54*(6), 639–643. https://doi.org/10.1080/02786826.2020.1751055

345 Feng, J. Q. (2023). Aerosol Deposition in 90° Circular Tube Bends with Laminar Flows: Effects of Inertial Impaction and

Gravitational Settling. *Aerosol Science and Engineering*, *7*(1), 107–117. https://doi.org/10.1007/s41810-022-00166-1

Friedlander, S. K., & Johnstone, H. F. (1957). Deposition of Suspended Particles from Turbulent Gas Streams. *Industrial & Engineering Chemistry*, *49*(7), 1151–1156. https://doi.org/10.1021/ie50571a039

Gormley, P. G., & Kennedy, M. (1948). Diffusion from a stream flowing through a cylindrical tube, *Proceedings of the Royal Irish Academy. Section A: Mathematical and Physical Sciences*, 52:163-169.

Grahn, P. (2024). COMSOL models for inertial deposition of particles in laminar flow. Zenodo. https://doi.org/10.5281/zenodo.11003261

Granek, H., Gras, J., & Paterson, D. (2003). The aerosol transmission efficiency of the Cape Grim Baseline Air Pollution Station 10 m sampling inlet. *Journal of Aerosol Science*, *34*(11), 1523–1537. https://doi.org/10.1016/S0021-8502(03)00118-6

Hangal, S., & Willeke, K. (1990). Aspiration efficiency: unified model for all forward sampling angles. *Environmental Science & Technology*, *24*(5), 688–691. https://doi.org/10.1021/es00075a012

Hapidin, D. A., Saputra, C., Maulana, D. S., Munir, M. M., & Khairurrijal, K. (2019). Aerosol chamber characterization for commercial particulate matter (PM) sensor evaluation. *Aerosol and Air Quality Research*, *19*(1), 181–194. https://doi.org/10.4209/aaqr.2017.12.0611

Karhu, J., Kuula, J., Virkkula, A., Timonen, H., Vainio, M., & Hieta, T. (2021). Cantilever-enhanced photoacoustic measurement of light-absorbing aerosols. *Aerosol Science and Technology*, *56*(1), 92–100. https://doi.org/10.1080/02786826.2021.1998338

Kulkarni, P., Baron, P. A., & Willeke, K. (2011). Aerosol Measurement: Principles, Techniques, and Applications: Third Edition. In P. Kulkarni, P. A. Baron, & K. Willeke (Eds.), *Aerosol Measurement: Principles, Techniques, and Applications: Third Edition: Vol. 1st editio* (2nd ed.). John Wiley & Sons, Inc. https://doi.org/10.1002/9781118001684

Kumar, P., Fennell, P., Symonds, J., & Britter, R. (2008). Treatment of losses of ultrafine aerosol particles in long sampling tubes during ambient measurements. *Atmospheric Environment*, *42*(38), 8819–8826. https://doi.org/10.1016/j.atmosenv.2008.09.003

Lelieveld, J., Pozzer, A., Pöschl, U., Fnais, M., Haines, A., & Münzel, T. (2020). Loss of life expectancy from air pollution compared to other risk factors: A worldwide perspective. *Cardiovascular Research*, *116*(11), 1910–1917. https://doi.org/10.1093/cvr/cvaa025

Linke, C., Ibrahim, I., Schleicher, N., Hitzenberger, R., Andreae, M. O., Leisner, T., & Schnaiter, M. (2016). A novel single-cavity three-wavelength photoacoustic spectrometer for atmospheric aerosol research, *Atmospheric Measurement Techniques*, 9, 5331–5346. https://doi.org/10.5194/amt-9-5331-2016

Liu, X., Fan, X., Zhao, Y., Duan, C., & Zhou, C. (2022). Particles movement behavior and apparent density in gas–solid fluidized bed as determined by an electronic dynamometer and electrical capacitance tomography. *Chemical Engineering Journal*, *429*, 132463. https://doi.org/10.1016/j.cej.2021.132463

Novosselov, I. V., Gorder, R. A., Van Amberg, J. A., & Ariessohn, P. C. (2014). Design and performance of a low-cost micro-

380     channel     aerosol     collector.     *Aerosol     Science     and     Technology*,     *48*(8),     822–830. https://doi.org/10.1080/02786826.2014.932895

Okazaki, K., Wiener, R. W., & Willeke, K. (1987). The combined effect of aspiration and transmission on aerosol sampling accuracy for horizontal isoaxial sampling. *Atmospheric Environment (1967)*, *21*(5), 1181–1185. https://doi.org/10.1016/0004-6981(87)90245-9

385     Pui, D. H., Romay-Novas, F., & Liu, B. Y. H. (1987). Experimental study of particle deposition in bends of circular cross section. *Aerosol Science and Technology*, *7*(3), 301–315. https://doi.org/10.1080/02786828708959166

Reineking, A., & Porstendörfer, J. (1986). Measurements of particle loss functions in a differential mobility analyzer (TSI, Model 3071) for different flow rates. *Aerosol Science and Technology*, *5*(4), 483–486. https://doi.org/10.1080/02786828608959112

390     Ren, J., Tang, M., & Novoselac, A. (2022). Experimental study to quantify airborne particle deposition onto and resuspension from clothing using a fluorescent-tracking method. *Building and Environment*, *209*(October 2021), 108580. https://doi.org/10.1016/j.buildenv.2021.108580

Tian, L., & Ahmadi, G. (2007). Particle deposition in turbulent duct flows-comparisons of different model predictions. *Journal of Aerosol Science*, *38*(4), 377–397. https://doi.org/10.1016/j.jaerosci.2006.12.003

395     Von Der Weiden, S. L., Drewnick, F., & Borrmann, S. (2009). Particle Loss Calculator - A new software tool for the assessment of the performance of aerosol inlet systems. *Atmospheric Measurement Techniques*, *2*(2), 479–494. https://doi.org/10.5194/amt-2-479-2009

Ye, Y., & Pui, D. Y. H. (1990). Particle deposition in a tube with an abrupt contraction. *Journal of Aerosol Science*, *21*(1), 29–40. https://doi.org/10.1016/0021-8502(90)90020-X

400     Yu, B., Peng, Y., Luo, X., Zhu, X., Gong, H., & Liu, Y. (2023). Effects of particle wettability and water moisture on separation efficiency and drop size distribution of particle-laden droplets in oil. *Colloids and Surfaces A: Physicochemical and Engineering Aspects*, *659*, 130790. https://doi.org/10.1016/j.colsurfa.2022.130790

Zuo, Y. Y., Uspal, W. E., & Wei, T. (2020). Airborne Transmission of COVID-19: Aerosol Dispersion, Lung Deposition, and Virus-Receptor Interactions. *ACS Nano*, *14*(12), 16502–16524. https://doi.org/10.1021/acsnano.0c08484

405